Sound speed profile characterization by the image source method

S. Pinson[a] and L. Guillon
Institut de Recherche de l'Ecole Navale (IRENav), BCRM Brest, CC 600, F-29240 Brest Cedex 9, France

(Received 11 December 2009; revised 20 July 2010; accepted 30 July 2010)

This paper presents the first results of an imaging technique that measures the geoacoustic structure of a seafloor in shallow water areas. The devices used were a broadband (100 Hz–6 kHz) acoustic source towed by a ship and a vertical array. Among all the acoustic paths existing in the water column, two are used: the direct one and the seabed-reflected one, the latter being composed of the reflections from the seafloor's surface as well as that from each buried layer. Due to the good time resolution of the signal and to the short range configuration, the reflected signal can be modeled as a sum of contributions coming from image sources relative to the seabed layers. The seabed geometry and the sound speed profile can then be recovered with the detection and localization of these image sources. The map of the image sources is obtained by a function that combines back-propagation of signals and knowledge of the emitted pulse. The thickness and sound-speed of each layer is finally obtained by a position analysis of the image sources. The results obtained by this data-driven algorithm on both at-sea and synthetic data are satisfactory.
 [DOI: 10.1121/1.3483720]

PACS number(s): 43.30.Ma, 43.30.Pc, 43.60.Fg, 43.60.Rw [NPC] Pages: 1685–1693

I. INTRODUCTION

Knowledge of seabed structure is essential to many applications. Complementarily to direct geophysics measurements, remote sensing by acoustics has prove its ability to get both the geometry and the physical characteristics of the seabed. Most of the present-day techniques are based on an inversion process such as, for example, matched field methods[1] or inversion of backscattering strength data.[2] In 2000, C. Holland and J. Osler proposed a joint time-frequency method based on reflection coefficient measurement at short distance.[3] In their measurements, they used a single hydrophone on a vertical array and a towed omnidirectional broadband source (Fig. 1). This data was also used recently to study the dependence of the coherence on the nature of the seabed.[4]

Based on this geometrical configuration, an imaging method to invert the seafloor structure (layering and sound speed profile) is presented in this paper. A classical imaging method used to image the seabed structure is the Kirchhoff migration[5] which consists of backpropagating recorded signals to geological interfaces (i.e., reflectors) that are equivalent in this case to extended sources. Here we consider these interfaces as acoustical mirrors on which images of the real source appear. The advantage of imaging the seafloor by searching for point sources is that it becomes possible to use high resolution array processing and then use the position of these image sources to determine the seabed structure without an inversion process. To that end, the full vertical array response with only one shot of the towed source is used.

The data used in this paper is presented on Section II. In Section III, the method with its hypothesis, its algorithm and results on synthetic and real data are described. Finally, Section IV explains how the sound speed profile can be obtain from the image source locations.

II. DATA AND MODEL

The configuration of the experiment is a broadband source (100 Hz–6 kHz) 20 cm bellow the sea surface and an array made of 15 hydrophones irregularly spaced over 64 m. The lowermost hydrophone is around 12 m above the seafloor (Fig. 1). For modeled data, the configuration is the same as for experimental data.

The physical phenomenon that leads to recovery of the sound speed profile is the refraction of sound waves in the layers. Then, when the range between source and receivers is long, the refraction phenomenon is high. The range also needs to be short enough to avoid a total reflection phenomenon on the interfaces which occurs at high incident angles. Here, with a 150 m water depth, the range between source and receivers for both real data and modeled data is 200 m, which is a good compromise. This distance leads to an incident angle of 45° on the seafloor for the middle of the array which is far from the critical angle.

A. Synthetic data

Synthetic data is obtained by a numerical evaluation of the Sommerfeld integral, the exact analytical solution of the reflection of a spherical wave on layered media.[6,7] The transfer function H_n of this reflection between a source located at $\mathbf{r}_0^s=(0,z_0^s)$ and a hydrophone n located at $\mathbf{r}_n^r=(r_n^r,z_n^r)$ is

$$H_n(\mathbf{r}_n^r,\mathbf{r}_0^s,\omega)=\mathrm{i}k\int_0^{\pi/2-\mathrm{i}\infty}\mathrm{J}_0(|r_0^s-r_n^r|k\sin\theta)R(\theta,\omega)\times \mathrm{e}^{\mathrm{i}k(z_n^r+z_0^s)\cos\theta}\sin\theta\,\mathrm{d}\theta, \quad (1)$$

[a]Author to whom correspondence should be addressed. Electronic mail: samuel.pinson@ecole-navale.fr

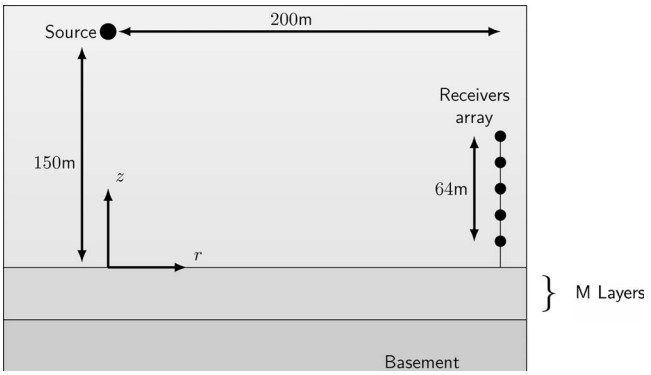

FIG. 1. Sketch of the experiment. The source is 200 m away from the vertical array. The receiver array, moored on the seafloor, is made of 15 hydrophones, is 64 m long. The lowermost hydrophone is around 12 m above the seafloor.

where θ is the angle of incidence, ω the angular frequency, and k the wave number. The exponents s and r respectively stand for a source and a receiver. Because this integral is the result of plane wave decomposition, the term $R(\theta,\omega)$ is the plane wave reflection coefficient and can be computed for an arbitrary layering of fluid or elastic media.[8] The time signal composed of the direct and the reflected wave at hydrophone n is

$$s_n(t) = \mathrm{FT}^{-1}\left[\left(\frac{e^{i\omega((|\mathbf{r}_0^s-\mathbf{r}_n^r|)/c_0)}}{|\mathbf{r}_0^s-\mathbf{r}_n^r|} + H_n(\mathbf{r}_n^r,\mathbf{r}_0^s,\omega)\right)\times F(\omega)\right], \tag{2}$$

where FT^{-1} is the inverse Fourier transform, $F(\omega)$ the emitted wavelet spectrum (Fig. 2) and $G_0(\mathbf{r}_1,\mathbf{r}_2,\omega)=e^{i\omega((|\mathbf{r}_1-\mathbf{r}_2|)/c_0)}/|\mathbf{r}_1-\mathbf{r}_2|$ the Green's function of an homogeneous medium with a wave number $k_0=\omega/c_0$, c_0 being the sound speed in water. Note that the signal used for the synthetic data comes from the real data experiments (see Section II B). The choice of the geoacoustic structure for the synthetic data is driven by two opposite principles: on the one hand, it should be complex enough to prove the validity of the method, but on the other hand, it should be simple enough to avoid difficult interpretation. The simulated seabed is composed of 9 fluid sediment layers covering a semi-infinite fluid basement (Table I). The synthetic data is then obtained with Eqs. (1) and (2), $R(\theta,\omega)$ being computed with these parameters.

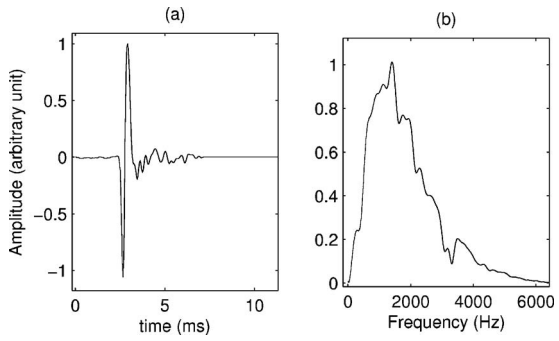

FIG. 2. Signal emitted by the source (a) in the time domain and (b) in the frequency domain.

TABLE I. Geoacoustic parameters for the synthetic data. The media used here are non-dissipative.

Layer	Sound speed (m/s)	Density	Thickness (m)
Water	1500	1	···
1	1520	1.1	3
2	1540	1.2	3.5
3	1600	1.5	4
4	1630	1.7	2
5	1700	1.9	6
6	1720	2	2
7	1800	2.5	5
8	1900	3	3
9	1920	3.1	2
Basement	2000	3.6	···

The temporal signal simulated for the 8th hydrophone of the array (Fig. 3) shows visible echoes from the 10 interfaces. Echoes from these interfaces are identified on Fig. 3. Using Eqs. (1) and (2), multiple reflections between interfaces are present in the computed signal but these echoes amplitudes are too small to be visible or to interfere with echoes from direct reflections.

B. Data from SCARAB experiment

The method developed here is also tested on real data acquired in June 1998 near Elba Island in Italy (Fig. 4, left) as part of the SCARAB (Scattering And ReverberAtion from the sea Bottom) experiment series (see Ref. 3 for details). The data used here are from site 2 where the water depth is 150 m and, from side-scan sonar data, the seabed is flat and featureless; bottom slopes are 0.3° or less. Geoacoustic inversion from broadband reflection data[3] shows sound speeds and densities consistent with a silty-clay sediment with intercalating sandy sediments (Fig. 4, right). One of the recorded signals is shown in Fig. 5. One can note the presence of a non-negligible additive noise but numerous seabed reflections are nevertheless still visible.

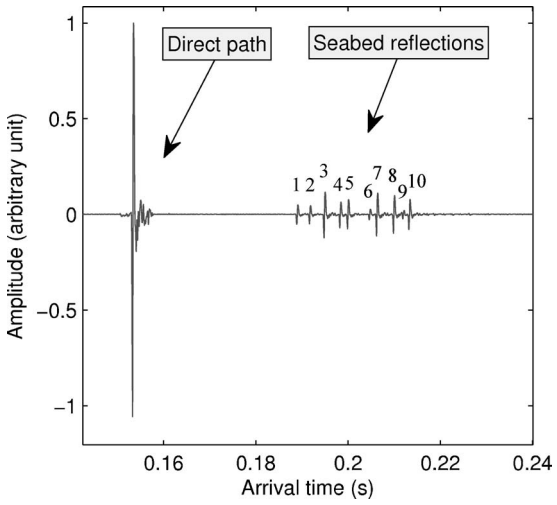

FIG. 3. Temporal signal computed for the 8th hydrophone of the array. Numbers 1–10 stand for interface reflections.

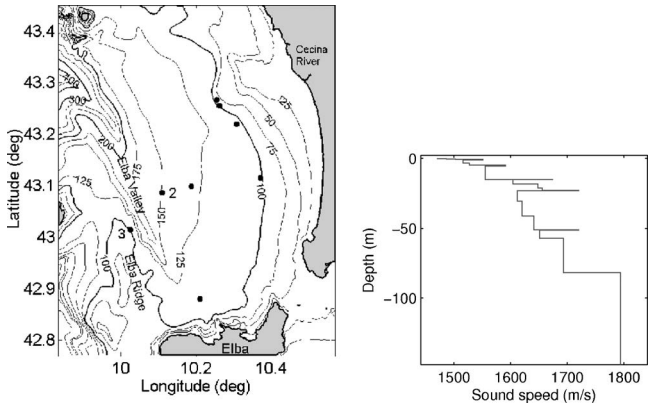

FIG. 4. Left: experiment area of the Scarab experiment. Right: sound speed profile obtained from inversion for site 2 (Ref. 3).

III. DETECTION OF IMAGE SOURCES

A. Image sources

The image source method is widely used to simulate wave propagation. It models the reflected wave as a wave emitted by the image source located symmetrically behind the reflecting interface. This method is generally used for room acoustics,[9] propagation in a waveguide[10,11] or to model the reflection from a half space of an emission from a radar antenna.[12] In these two last cases, the image source coordinates are complex in order to take into account the angular variations of the reflection coefficient.

This method based on the ray theory is usually used to model systems, but according to the author's knowledge, not for performing a characterization. The ray theory is used in some geoacoustic inversion techniques[13–15] but two main differences exist with the image source method. First, in these works the geometric approximation is used to compute travel times or amplitudes of arrival but the image sources are not sought. Second, the image source method does not perform an inversion in the sense of the optimization of a cost function. It is more similar to a measurement method. If the sound speed and thickness of each layer in the model seabed were set to their correct values, the image sources will be backpropagated to their proper positions. Given that the source image positions are known, the layer properties may be found.

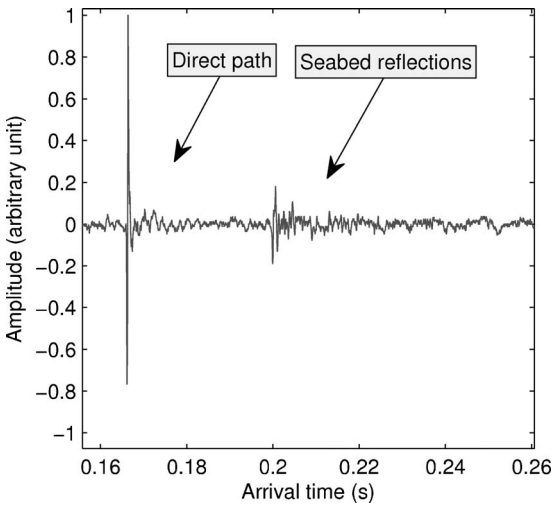

FIG. 5. Temporal signal recorded at the 8th hydrophone of the array.

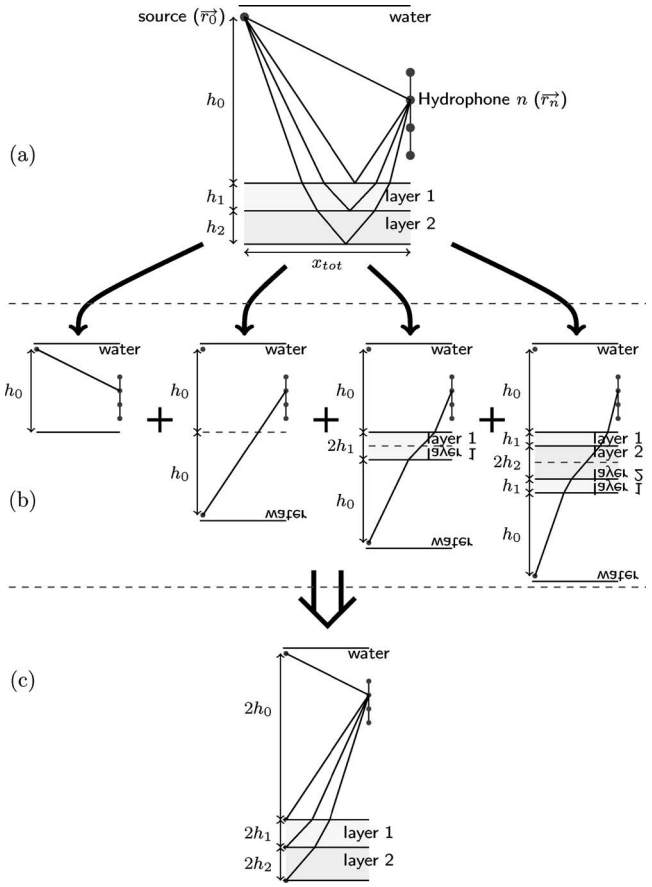

FIG. 6. Modeling of the seafloor with image sources: (a) original configuration, (b) each reflection on an interface is replaced by its image source, (c) the final equivalent system.

To model the reflection of the emitted wave as a collection of image sources, the following points are assumed:

- the water column and the geologic layers are homogeneous, the latter being all horizontal,
- the angle of incidence at an interface is smaller than the critical angle, and its angular variation (measured on the array for a given source-array distance) is small enough to neglect its influence on the reflection coefficient,
- only the first reflections are taken into account; multiple reflections between interfaces are considered too low in amplitude to interfere with the first ones and be detectable,
- the layer reflections are coherent.

In this case, each reflection on an interface [Fig. 6(a)] is identified by the receiver array as an image source which can be described in an equivalent system: the structure (water +sediment layers) above this interface and its symmetric structure [Fig. 6(b)]. So, each image is represented in a different equivalent system but, for any given system, the places of the components (water and layer and their symmetric structure) have no consequences on the angle of arrival or on the total travel time. It is then possible to merge all the equivalent systems in a single one which contains all the

image sources [Fig. 6(c)]. In this system, all the thicknesses are doubled and the images are located on the interfaces and at a zero horizontal offset relative to the source.

B. Backpropagation of signals

The geoacoustic inversion by the image source method requires a very accurate localization. To solve this problem, the recorded signals are backpropagated numerically in the water without the sediment structure. This can be done in this case because the time t_0 of the emission of the wavelet by the source is known and because the time resolution of signal is good enough to separate each reflection (Figs. 3 and 5).

The imaging with backpropagation of signals is very close to the time reversal in a homogeneous media[16–19] but signals reflected by the seabed will not focus only on the real source after backpropagation like in the physical time reversal.[20] They will also focus on all image sources corresponding to the reflections on geological interfaces because the sediment structure is suppressed. This phenomenon has already been shown during a time reversal experiment[21] but here, it is used to characterize the seafloor. Source and images are coherent because they emit the same signal (with different amplitudes) at time t_0.

For a monopole emitting a short pulse $f(t)$ at $\mathbf{r}_0^s$ in a homogeneous and isotropic medium, the received signal at hydrophone n at $\mathbf{r}_n^r$ is

$$s_n(t) = f(t) * g(\mathbf{r}_0^s, \mathbf{r}_n^r, t) + \eta_n(t), \tag{3}$$

where $*$ is the convolution product, $g(\mathbf{r}_0^s, \mathbf{r}_n^r, t)$ the temporal domain Green's function, and $\eta_n(t)$ an additive supposed spatially white noise.

If $M+1$ monopole sources (the real one$+M$ images) emit the same wavelet at the same time with a different amplitude factor β_m, the received signal becomes

$$s_n(t) = \sum_{m=0}^{M} \beta_m f(t) * g(\mathbf{r}_m^s, \mathbf{r}_n^r, t) + \eta_n(t), \tag{4}$$

or in the frequency domain

$$S_n(\omega) = \sum_{m=0}^{M} \beta_m F(\omega) \times G(\mathbf{r}_m^s, \mathbf{r}_n^r, \omega) + \eta_n(\omega), \tag{5}$$

with $G(\mathbf{r}_m^s, \mathbf{r}_n^r, \omega)$ and $F(\omega)$ the Fourier transforms of $g(\mathbf{r}_0^s, \mathbf{r}_n^r, t)$ and $f(t)$.

To backpropagate signals at a search point $\mathbf{r}$, the spectrum $S_n(\omega)$ is multiplied by the inverse Green function in an homogeneous medium (with sound speed c_0) $G_0^{-1}(\mathbf{r}, \mathbf{r}_n^r, \omega) = |\mathbf{r} - \mathbf{r}_n^r| \times e^{-i\omega((|\mathbf{r}-\mathbf{r}_n^r|)/c_0)}$:

$$S_{bn}(\mathbf{r}, \omega) = \left[\sum_{m=0}^{M} \beta_m F(\omega) \times G(\mathbf{r}_m^s, \mathbf{r}_n^r, \omega) + \eta_n(\omega) \right] \times G_0^{-1}(\mathbf{r}, \mathbf{r}_n^r, \omega). \tag{6}$$

In order to reduce the influence of all sources and the noise, the backpropagated signals are windowed around t_0 with a smooth window $w(t)$ that has nearly the same duration than the emitted wavelet. In the frequency domain, the windowed backpropagated signal is

$$S_{wn}(\mathbf{r}, \omega) = S_{bn}(\mathbf{r}, \omega) * \mathrm{FT}[w(t)]. \tag{7}$$

Then, the average of the N hydrophones of the array is computed and the result (homogeneous to a pressure) is mapped as follows:

$$\mathcal{I}^{BW}(\mathbf{r}) = \sqrt{\int_{-\infty}^{+\infty} \left| \frac{1}{N} \sum_n S_{wn}(\mathbf{r}, \omega) \right|^2 \mathrm{d}\omega}. \tag{8}$$

Equivalently, $\mathcal{I}^{BW}(\mathbf{r})$ can be noted as a sum of the covariance matrix elements:

$$\mathcal{I}^{BW}(\mathbf{r}) = \sqrt{\int_{-\infty}^{+\infty} \frac{1}{N} \sum_{n=1}^{N} \sum_{q=1}^{N} S_{wn}(\mathbf{r}, \omega) S_{wq}^*(\mathbf{r}, \omega) \mathrm{d}\omega}, \tag{9}$$

where $S_{wn}^*(\mathbf{r}, \omega)$ is the conjugate of $S_{wn}(\mathbf{r}, \omega)$.

$\mathcal{I}^{BW}$ is very close to the Kirchhoff migration but here, instead of migrating signals on the reflectors, they are migrated to the image source locations.

Even with the window, there is still speckle on $\mathcal{I}^{BW}$. Indeed, the wavelet emitted by the source m and received by the sensor n draws a circle on the map centered on the sensor with a radius of $|\mathbf{r}_0^s - \mathbf{r}_n^r|$. The intersection of the circles of the N sensors corresponds to the location of a source. The problem is that it is possible for some isolated circles to be greater than a coherent intersection of circles corresponding to another source with a lower amplitude. This is visible on Figs. 7(a) and 7(b) where the functional $\mathcal{I}^{BW}(\mathbf{r})$ is computed respectively for synthetic and real data. For the synthetic data, the map clearly shows the sources but also all the circles drawn by all the individual hydrophones as mentioned. The same result is observed on SCARAB data [Fig. 7(b)] where the image obtained with $\mathcal{I}^{BW}(\mathbf{r})$ shows even more artifacts. This may have been caused by the presence of another sound-emitting object (maybe a merchant ship) near the experiment area. With this map of image sources, it is difficult to locate them accurately.

C. Projection onto the orthogonal subspace and range estimation

The source amplitudes are not required for localization. Consequently the backpropagated and windowed signals can be normalized and projected onto the orthogonal subspace $(\mathbf{I} - [\mathbf{S}_w(\mathbf{r}, \omega)/\|\mathbf{S}_w(\mathbf{r}, \omega)\|_{2,N}][\mathbf{S}_w^H(\mathbf{r}, \omega)/\|\mathbf{S}_w(\mathbf{r}, \omega)\|_{2,N}])$. Then, source locations correspond to the minima of the function

$$\mathcal{F}^{OS}(\mathbf{r}, \omega) = \mathbb{I}^H \left(\mathbf{I} - \frac{\mathbf{S}_w(\mathbf{r}, \omega)}{\|\mathbf{S}_w(\mathbf{r}, \omega)\|_{2,N}} \frac{\mathbf{S}_w^H(\mathbf{r}, \omega)}{\|\mathbf{S}_w(\mathbf{r}, \omega)\|_{2,N}} \right) \mathbb{I} \tag{10}$$

or

$$\mathcal{F}^{OS}(\mathbf{r}, \omega) = N - \sum_{n=1}^{N} \sum_{q=1}^{N} \frac{S_{wn}(\mathbf{r}, \omega)}{\|\mathbf{S}_w(\mathbf{r}, \omega)\|_{2,N}} \times \frac{S_{wq}^*(\mathbf{r}, \omega)}{\|\mathbf{S}_w(\mathbf{r}, \omega)\|_{2,N}}, \tag{11}$$

where subscript ^{H} denotes the Hermitian transpose,

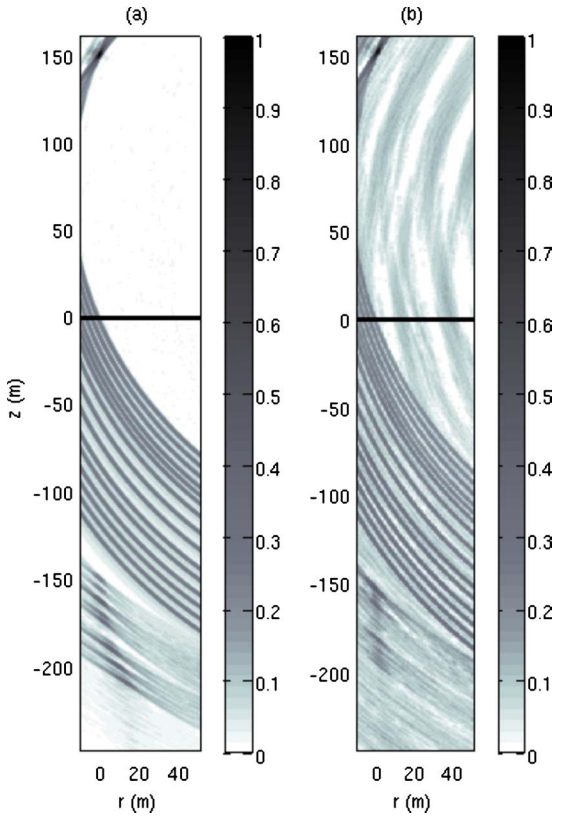

FIG. 7. (Color online) Focus on the image sources using $\mathcal{I}^{BW}$ for (a) the synthetic model and (b) the SCARAB data. The source is at (r=0, z =150) and the solid line at z=0 represents the seafloor. The array is not drawn on the picture and is at r=200 m.

$$\mathbf{S}_w(\mathbf{r},\omega)=\begin{pmatrix} S_{w1}(\mathbf{r},\omega) \\ S_{w2}(\mathbf{r},\omega) \\ \vdots \\ S_{wN}(\mathbf{r},\omega) \end{pmatrix},$$

$\|\cdot\|_{2,N}$ is the L^2 norm of the signal vector, $\mathbf{I}$ is identity matrix and $\mathbb{I}$ a column vector of ones.

One can note the similarity between Eq. (10) and the MUltiple SIgnal Classification (MUSIC)[22] algorithm. Here, the vectors of Green's function are replaced by vectors of ones because vectors of signals $\mathbf{S}_w$ are already backpropagated. Thus, $\mathbf{S}_w$ with its normalization and windowing can be interpreted as a user-selected set of eigenvectors of the signals. This is possible here because all reflected pulses in the temporal signal are in the same order for each sensor. The advantage of this method is that there is no limitation of the number of sources detectable in opposition to the MUSIC algorithm in which it is impossible to find more sources than the number of sensors. In the MUSIC algorithm with wideband sources, the information of the eigenvectors is redundant as a function of frequency even if several echoes with different arrival times are visible by eye on the temporal signal (see Fig. 3). The range resolution of $\mathcal{F}^{OS}$ is directly linked to the window size $w(t)$. To improve the accuracy of the range resolution, we use the knowledge of the emitted wavelet $F(\omega)$ by comparing it with the average of the back-

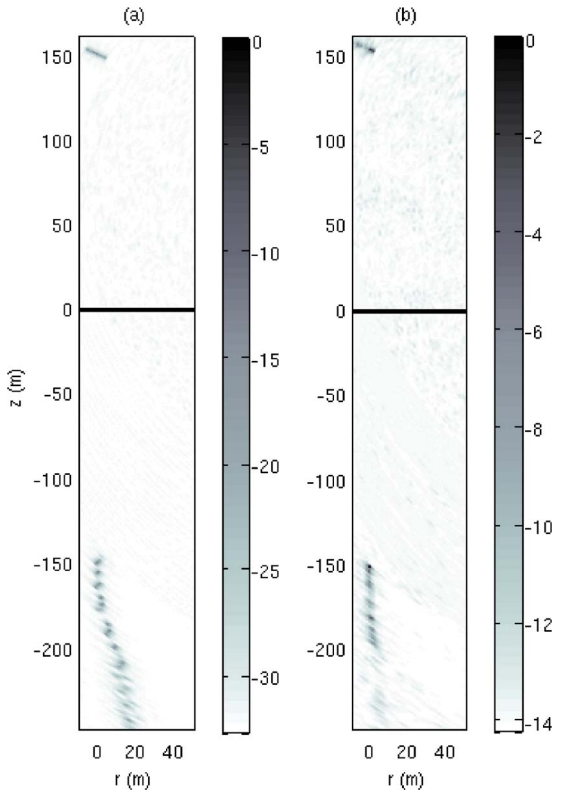

FIG. 8. (Color online) Focus on the image sources using $\mathcal{I}^{OSAT}(\mathbf{r})$ (in dB) for (a) the synthetic model and (b) the SCARAB data.

propagated and windowed signals. This comparison is very close to an arrival time analysis of the emitted pulse. For this operation, the function to minimize is

$$\mathcal{F}^{AT}(\mathbf{r},\omega)=\min_{\pm}\left|\frac{F_w(\omega)}{\|f_w(t)\|_{\infty,t}}\pm\frac{1}{N}\sum_n\frac{S_{wn}(\mathbf{r},\omega)}{\|s_{wn}(\mathbf{r},t)\|_{\infty,t}}\right|^2, \quad (12)$$

with $f_w(t)=f(t)\times w(t)$, $F_w(\omega)=\mathrm{FT}[f_w(t)]$, $s_{wn}(\mathbf{r},t)=\mathrm{FT}^{-1}[S_{wn}(\mathbf{r},\omega)]$ and $\|\cdot\|_{\infty,t}$ is the infinite norm of the signal over the time. The minimum is taken between addition and subtraction because the reflection coefficient may be positive or negative. Finally, the image sources are mapped with the function

$$\mathcal{I}^{OSAT}(\mathbf{r})=\frac{1}{\int_{-\infty}^{+\infty}|F_w(\omega)|^2\mathcal{F}^{OS}(\mathbf{r},\omega)+\mathcal{F}^{AT}(\mathbf{r},\omega)\mathrm{d}\omega}, \quad (13)$$

where $\mathcal{F}^{OS}(\mathbf{r},\omega)$ is compensated in frequency with the power spectrum of the emitted pulse.

The results of the function $\mathcal{I}^{OSAT}(\mathbf{r})$ [Eq. (13)] are displayed on Fig. 8(a) for synthetic data and on Fig. 8(b) for the at-sea data.

This new function eliminates all the circles drawn with $\mathcal{I}^{BW}(\mathbf{r})$ [Eq. (9)] and the image sources appear very clearly and with a good resolution both in range and angle. Because of the low frequency regime of the source, it appears from the map obtained with real data that phase shifting from dispersion phenomena is not strong enough to influence $\mathcal{F}^{AT}(\mathbf{r})$ and reduce the quality of the detected images. On this SCARAB data result, fewer image sources appear on the

map than expected from the knowledge of the geoacoustic structure of the seafloor (made of 20 layers with a total thickness of 150 m) because some of the layers are very thin and their corresponding image sources are merged in a single spot. The map obtained with synthetic data shows more than ten image sources, some of them correspond to multiple reflections between interfaces. On the temporal signal they correspond to very low amplitude echoes that could be hidden by a faint noise. Nevertheless, their amplitudes on the map are lower than images corresponding to the first reflections and can be eliminated from the automated detection by adjusting a threshold. One can note on the maps that the image sources are not aligned on a perfect straight line; this is due to the refraction in the sediment layer (cf. Figure 6) that is not yet taken into account in the detection algorithm.

IV. SOUND SPEED PROFILE MEASUREMENT

As described in Section III C, image sources are not aligned on the vertical axis because signals are backpropagated in water without sediment structure. To find the layer sound speed, image sources must be aligned on the vertical axis of the real source. This vertical axis is the line between the real source and the first image, meaning that finding the real source and the first image makes it possible to calculate the array tilt and correct it.

A. Correction of the array tilt

Because of currents, it is possible for the vertical array to be deformed. If one assumes that the deformation is mainly a tilt, the array makes an angle α with the vertical. If this angle is not included in the coordinates of the hydrophones, the line between the real source and the first image forms an angle—α with the real vertical line. Thus, the new coordinates of the hydrophones $\mathbf{r}_n^{r\alpha}=(r_n^{r\alpha},z_n^{r\alpha})$ that include the tilt are

$$r_n^{r\alpha}=r_n^r\cos\alpha-z_n^r\sin\alpha,$$

$$z_n^{r\alpha}=r_n^r\sin\alpha+z_n^r\cos\alpha, \tag{14}$$

with

$$-\alpha=\tan^{-1}\frac{r_0^s-r_1^s}{z_0^s-z_1^s}. \tag{15}$$

(r_0^s,z_0^s) and (r_1^s,z_1^s) are respectively the real source and the first image's coordinates found with the tilted array.

The array tilt is usually an unknown parameter and is easily recovered here with the image source method. After tilt correction, image sources can be aligned on the vertical real source axis to recover the sound speed profile. Note that the vertical axis is not perpendicular to the sea surface but to the seabed.

B. Image source alignment

When $\mathcal{I}^{OSAT}(\mathbf{r})$ [Eq. (13)] is computed with correct sound speeds from c_0 to c_{l-1} and a wrong one $\tilde{c}_l$ in layer l the $(l+1)^{th}$ image is located at $\mathbf{r}=(\tilde{r}_{l+1}^s,\tilde{z}_{l+1}^s)$ with $\tilde{r}_{l+1}^s\neq r_0^s$ (Fig. 9). The $\tilde{}$ symbol indicates an incorrect value.

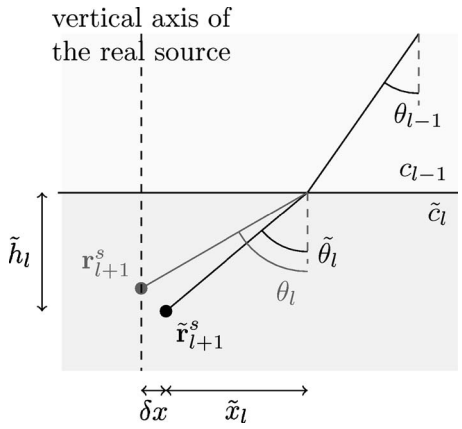

FIG. 9. Image sources gap to the vertical of the real source.

The range gap $\delta x=\tilde{r}_{l+1}^s-r_0^s$, the apparent depth $\tilde{h}_l$, and the angle of arrival on the array center θ_0 of this image give all the necessary information to find the real sound speed in the layer. The Snell-Descartes law allows one to obtain the arrival angle $\tilde{\theta}_l$ on the image source:

$$\tilde{\theta}_l=\sin^{-1}\left(\frac{\tilde{c}_l}{c_0}\sin\theta_0\right), \tag{16}$$

then, the horizontal travel $\tilde{x}_l$ in the layer is

$$\tilde{x}_l=\tilde{h}_l\tan\tilde{\theta}_l, \tag{17}$$

and the travel time in the layer t_l is

$$t_l=\frac{\tilde{h}_l}{\tilde{c}_l\cos\tilde{\theta}_l}. \tag{18}$$

Even if $\tilde{\theta}_l$, $\tilde{h}_l$ and $\tilde{c}_l$ are incorrect, t_l is the correct travel time in the layer for that ray because of the backpropagation procedure. The real horizontal travel in the layer that is $x_l=\tilde{x}_l+\delta x$ is also known. With these two quantities and the Snell-Descartes law, it is now possible to write

$$\frac{\sin\theta_0}{c_0}=\frac{\sin\tilde{\theta}_l}{\tilde{c}_l}=\frac{\sin\hat{\theta}_l}{\hat{c}_l}=\frac{(\tilde{x}_l+\delta x)}{t_l\hat{c}_l}\frac{1}{\hat{c}_l}, \tag{19}$$

where the symbol $\hat{}$ indicates an estimated value. Thus, the estimated sound speed in the layer l is

$$\hat{c}_l=\sqrt{\frac{(\tilde{x}_l+\delta x)c_0}{t_l\sin\theta_0}}. \tag{20}$$

The estimation is due to the ray path approximated as coming from the array center.

C. Focus in layers

To compute $\mathcal{I}^{OSAT}(\mathbf{r})$ [Eq. (13)] taking into account the layer sound speeds $c_0,\ldots,c_{l-1},\hat{c}_l$, the inverse Green's function that takes into account the refraction in layers is approximated by

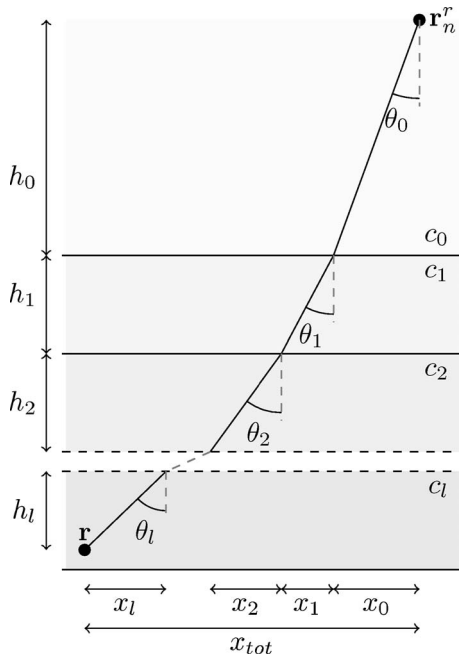

FIG. 10. Refraction of ray in layered media.

$$G^{-1}(\mathbf{r}_n^r,\mathbf{r},\omega) = D_{tot}(\mathbf{r}_n^r,\mathbf{r}) \times e^{-i\omega\Delta t(\mathbf{r}_n^r,\mathbf{r})}, \tag{21}$$

where $D_{tot}(\mathbf{r}_n^r,\mathbf{r})$ is the path length between $\mathbf{r}_n^r$ and $\mathbf{r}$ (Fig. 10) and $\Delta t(\mathbf{r}_n^r,\mathbf{r})$ is the travel time. The expressions of D_{tot} and Δt are[6]

$$D_{tot} = \sum_{p=0}^{l} \frac{h_p}{\cos\,\theta_p} = \sum_{p=0}^{l} \frac{h_p}{\sqrt{1-\left(\frac{c_p}{c_0}\sin\,\theta_0\right)^2}}, \tag{22}$$

$$\Delta t = \sum_{p=0}^{l} \frac{h_p}{c_p\cos\,\theta_p} = \sum_{p=0}^{l} \frac{h_p}{c_p \times \sqrt{1-\left(\frac{c_p}{c_0}\sin\,\theta_0\right)^2}}, \tag{23}$$

where h_p and θ_p are respectively the thickness and the incidence angle of the layer p (Fig. 10). To find these values, the initial incidence angle θ_0 must be known. The horizontal distance covered by a ray between two different horizontal planes is[6]

$$x(\theta_0) = \sum_{p=0}^{l} h_p \tan\,\theta_p = \sum_{p=0}^{l} \frac{h_p\frac{c_p}{c_0}\sin\,\theta_0}{\sqrt{1-\left(\frac{c_p}{c_0}\sin\,\theta_0\right)^2}}, \tag{24}$$

and the horizontal travel between $\mathbf{r}_n^r=(r_n^r,z)$ and $\mathbf{r}=(r,z)$ is $x_{tot}=|r_n^r-r|$. Then, θ_0 is found by solving

$$x(\theta_0) - x_{tot} = 0. \tag{25}$$

Then the inverse Green's function [Eq. (21)] is used for the backpropagation of signals in Eq. (6).

D. Algorithm

Once the tilt is corrected and the first image is found with $\mathcal{I}^{OSAT}(\mathbf{r})$, the first layer sound speed $\tilde{c}_1$ is initialized with that of water. When the second image is located, $\hat{c}_1$ is calculated and $\mathcal{I}^{OSAT}(\mathbf{r})$ restarts the search of the second image with this new sound speed of the first layer. Then, if δx of the second image is still different from zero, $\hat{c}_1$ becomes $\tilde{c}_1$ and a new estimate $\hat{c}_1$ is calculated. This process is done until $\delta x=0$. Then $\hat{c}_1$ becomes c_1 and $\tilde{c}_2$ is initialized with c_1 and the operation is repeated for each layer.

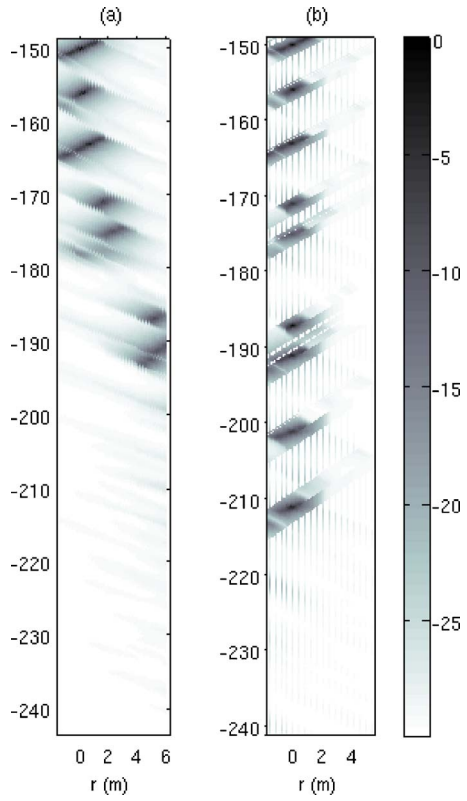

FIG. 11. (Color online) Image sources before (a) and after (b) alignment for the synthetic data.

E. Results

In order to recover the sound speed profile, image sources have to be precisely located. This is done using a dense spatial mesh. Here the density of the mesh is one node each 10 cm (a tenth of the wavelength at the central frequency) on the ray coming from the array center and these ray paths cross the vertical source axis every 10 cm. Then the alignment of images (Fig. 11) allows one to recover the sound speed profile. It is correctly recovered for the synthetic data where only the 9th interface is not found because of its low impedance contrast [Fig. 12(a)].

Ground truth from SCARAB experiment[3] has been obtained for the 6 first meters which is not enough to compare with the sound speed profile obtained with the image source method. So the result is compared with that of Holland and Osler. They obtained 20 layers (labeled with numbers from 1 to 20 in Table II) while the image source method obtains 11 layers (labeled with letters from *a* to *k* in Table II). The first meters of seafloor are complex (layers 1 to 5) with the notable presence of a thin surficial layer with a sound-speed gradient starting with a sound speed lower than water. In these first meters, the image source method gives 4 layers (*a*

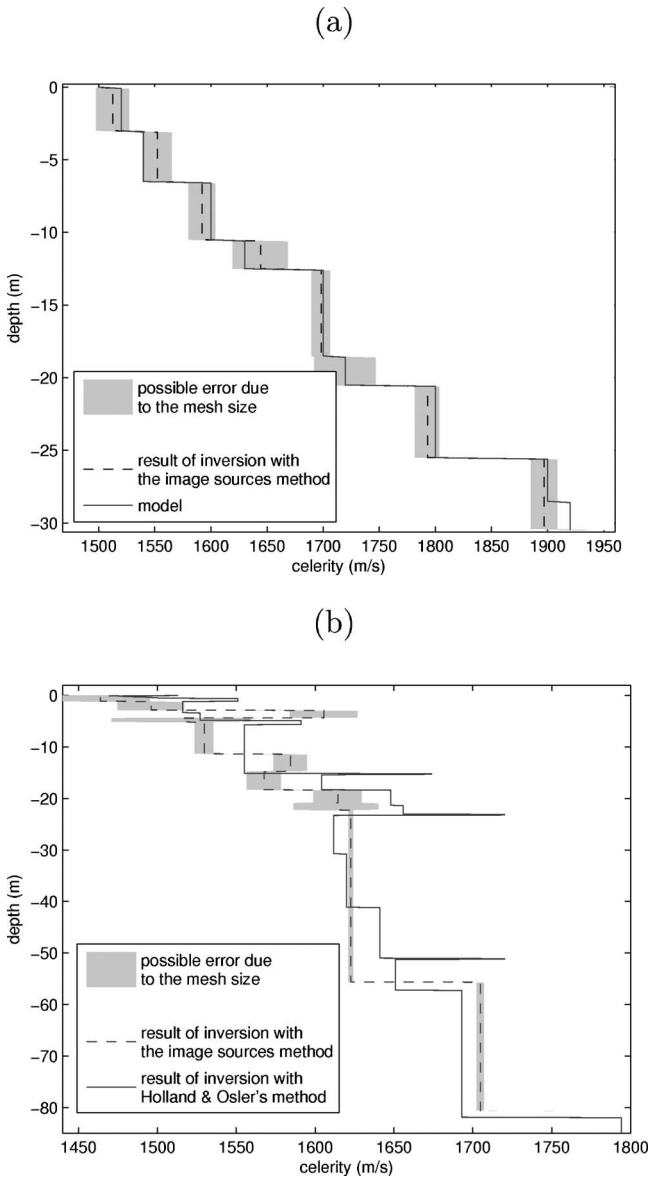

FIG. 12. Sound speed profiles found with the synthetic data (a) and with the real data (b) (see Ref. 3 for details).

to *d*) which depths match correctly with layers 2 to 5. However, the inverted speed profile is different from that of Holland and Osler. One can note that the two first layers (*a* and *b*) are found with a low sound speed which may corresponds to the surficial layer. Two layers (*e* and *f*) found by the image source method correspond to a single one (layer 6). Layers 7, 11, and 15 are not found probably because of their thinnesses (20 cm). Layers 8 to 10 are correctly enough found by image source method (layers *g* to *i*), the thickness differences being lower than 60 cm and the sound-speed differences being lower than 42 $\mathrm{m/s^{-1}}$. Layers 12 to 16 are merged in a single layer *j*. The obtained sound speed for layer *j* corresponds within an uncertainty of 10 $\mathrm{m/s^{-1}}$ to the mean sound speed of layers 12 to 16. The fusion of these layers is probably due to a low impedance contrast between successive layers which leads to a too low reflection coefficient to produce a detectable image source. The agreement between layer 17 and layer *k* is good for both the thickness and the sound speed.

TABLE II. Comparison of results with measured data between Holland's and image source method.

Holland and Osler's method				Image source method			
Layer	Thickness (m)	Depth (m)	Sound speed (m/s)	Layer	Thickness (m)	Depth (m)	Sound speed (m/s)
1	0.5	0.5	1470–1502				
2	0.6	1.1	1551	*a*	1.1	1.1	1464
3	2.2	3.3	1516	*b*	1.7	2.8	1496
4	1.5	4.8	1527	*c*	1.5	4.3	1606
5	0.8	5.6	1591	*d*	0.8	5.1	1516
				e	6.2	11.3	1530
6	9.5	15.1	1555	*f*	3.5	14.7	1584
7	0.2	15.3	1674				
8	3	18.3	1604	*g*	3.6	18.3	1568
9	3	21.3	1648	*h*	2.5	20.8	1615
10	1.7	23	1656	*i*	1.5	22.2	1614
11	0.2	23.2	1720				
12	7.5	30.7	1612				
13	10.4	41.1	1620				
14	9.9	51	1641				
15	0.2	51.2	1720				
16	6	57.2	1651	*j*	33.3	55.6	1622
17	24.7	81.9	1693	*k*	25	80.6	1705
18	68	149.9	1794				
19	0.2	150.1	1900				
20	⋯	⋯	1820				

The deepest layers 18, 19, and 20 are not found with the image source method. Despite these differences, the overall shapes of the sound speed profiles match correctly enough [Fig. 12(b)] and the profile given by the image source method is obtained without any *a priori* information about the number of layers, their thicknesses or their sound speed.

The sources of error in sound speed values are not studied here but on Fig. 12, the gray zones represent the maximum error for sound speeds when they are computed assuming that the maximum in amplitude of a detected image could be badly located and should be on a neighboring node. One can see that when layers are thin, errors are likely because of the mesh size. Among other sources of error, the successive determination of sound speeds in layers involves that a computed sound speed must compensate errors done with previous ones. Also, we suppose that the small size of the Fresnel zones (≈70 m) in the image source method makes the technique sensitive to the slopes (or low frequency roughness) of interfaces. The sensitivity to these parameters is the object of future work.

V. CONCLUSION

The initial results obtained on synthetic and real data with only one transmission between the source and the vertical array are promising. The different reflections on the interfaces are well modeled by image sources and the array process is able to locate them accurately enough to obtain the sound speed profile. The comparison of the real data result with another method shows significant differences but the global shapes of the sound speed profiles match correctly

enough. The main difference with existing methods is that the process presented here is not based on comparison with a model. It is a data-driven approach which consequently has a low computational cost and is very fast. It could therefore be used as a first step in a more accurate inversion procedure, or to evaluate the geologic structure and the sound speed profile of large areas with the use of a towed horizontal array. The object of future work is to find other parameters like density and low frequency roughness (or local slopes of interfaces).

ACKNOWLEDGMENTS

The authors wish to gratefully acknowledge Charles W. Holland for providing the data and for helpful discussion and remarks on the manuscript. They also thank the North Atlantic Treaty Organization Underwater Research Center under whose auspices the data were collected. This work is partially funded by the GIS-Europole Mer research consortium.

[1]A. Baggeroer, W. Kuperman, and P. Mikhalevsky, "An overview of matched field methods in ocean acoustics," IEEE J. Ocean. Eng. **18**, 401–424 (1993).
[2]D. Jackson and M. Richardson, *High-Frequency Seafloor Acoustics* (Springer, New York, 2007), pp. 321–330.
[3]C. Holland and J. Osler, "High resolution geoacoustic inversion in shallow water: A joint time and frequency domain technique," J. Acoust. Soc. Am. **107**, 1263–1279 (2000).
[4]L. Guillon and C. Holland, "Cohérence des signaux réfléchis par le sol marin: Modèle numérique et données expérimentales (Coherence of signals reflected by the seafloor: Numerical modeling vs experimental data)," Trait. Signal **25**, 131–138 (2008).
[5]J. Claerbout and S. Doherty, "Downward continuation of moveout-corrected seismograms," Geophysics **37**, 741–768 (1972).
[6]L. Brekhovskikh and Y. Lysanov, *Fundamentals of Ocean Acoustics* (Springer-Verlag, Berlin, 1991), pp. 74–81.
[7]L. Brekhovskikh and O. Godin, *Acoustics of Layered Media. II: Point Sources and Bounded Beams* (Springer-Verlag, Berlin, 1999), pp. 1–15.
[8]P. Cervanka and P. Challande, "A new efficient algorithm to compute the exact reflection and transmission factors for plane waves in layered absorbing media (liquids and solids)," J. Acoust. Soc. Am. **89**, 1579–1589 (1991).
[9]J. Allen and D. Berkley, "Image method for efficiently simulating small room acoustics," J. Acoust. Soc. Am. **65**, 943–950 (1979).
[10]J. Fawcett, "Complex-image approximations to the half-space acousto-elastic Green's function," J. Acoust. Soc. Am. **108**, 2791–2795 (2000).
[11]J. Fawcett, "A method of images for a penetrable acoustic waveguide," J. Acoust. Soc. Am. **113**, 194–204 (2003).
[12]X. Xu and Y. Huang, "An efficient analysis of vertical dipole antennas above a lossy half-space," Electromagn. Waves **74**, 353–377 (2007).
[13]N. Chapman, J. Desert, A. Agarwal, Y. Stephan, and X. Demoulin, "Estimation of seabed models by inversion of broadband acoustic data," Acta. Acust. Acust. **88**, 756–759 (2002).
[14]C. Park, W. Seong, P. Gerstoft, and M. Siderius, "Time-domain geoacoustic inversion of high-frequency chirp signal from a simple towed system," IEEE J. Ocean. Eng. **28**, 468–478 (2003).
[15]P. Pignot and N. Chapman, "Tomographic inversion of geoacoustic properties in a range-dependent shallow-water environment," J. Acoust. Soc. Am. **110**, 1338–1348 (2001).
[16]P. Roux and W. Kuperman, "Time reversal of ocean noise," J. Acoust. Soc. Am. **117**, 131–136 (2005).
[17]L. Borcea, G. Papanicolaou, C. Tsogka, and J. Berryman, "Imaging and time reversal in random media," Inverse Probl. **18**, 1247–1279 (2002).
[18]L. Borcea, G. Papanicolaou, and C. Tsogka, "Optimal illumination and wave form design for imaging in random media," J. Acoust. Soc. Am. **122**, 3507–3518 (2007).
[19]J. Berryman, L. Borcea, G. Papanicolaou, and C. Tsogka, "Statistically stable ultrasonic imaging in random media," J. Acoust. Soc. Am. **112**, 1509–1522 (2002).
[20]M. Fink, "Time reversal mirrors," J. Phys. D: Appl. Phys. **26**, 1333–1350 (1993).
[21]C. Prada, J. de Rosny, D. Clorennec, J. Minonzio, A. Aubry, M. Fink, L. Berniere, P. Billand, S. Hibral, and T. Folegot, "Experimental detection and focusing in shallow water by decomposition of the time reversal operator," J. Acoust. Soc. Am. **122**, 761–768 (2007).
[22]R. Schmidt, "A signal subspace approach to multiple emitter and signal parameter estimation," Ph.D. thesis, Stanford University, Stanford, CA (1981).